Applied Catalysis B: Environmental 320 (2023) 121991

Contents lists available at ScienceDirect

Applied Catalysis B: Environmental

journal homepage: www.elsevier.com/locate/apcatb

Synergistic effect and nanostructure engineering of three-dimensionally hollow mesoporous spherical Cu_3P/TiO_2 in aqueous/flexible Zn–air batteries

Man Guo [a,1], Zhiyang Huang [a,1], Yuan Qu [a], Lixia Wang [a], Huatong Li [a], Tayirjan Taylor Isimjan [b,*], Xiulin Yang [a,*]

[a] Guangxi Key Laboratory of Low Carbon Energy Materials, School of Chemistry and Pharmaceutical Sciences, Guangxi Normal University, Guilin 541004, China
[b] Saudi Arabia Basic Industries Corporation (SABIC) at King Abdullah University of Science and Technology (KAUST), Thuwal 23955-6900, Saudi Arabia

ARTICLE INFO

Keywords:
Electron/mass transfer
Cu_3P/TiO_2
Hollow mesoporous structure
Zn-air battery
Flexible

ABSTRACT

Designing materials with electron/mass transfer effectively improves catalytic activity by synergistic effects between different species. Herein, we report a high-temperature pyrolysis strategy to induce charge transfer of Cu_3P loaded TiO_2 3D hollow mesoporous carbon nanospheres (Cu_3P/TiO_2@NC). Density functional theory (DFT) calculations disclose that synergistic between Cu_3P and TiO_2 can optimize the adsorption of oxygen intermediates and endow fast reaction kinetics. Cu_3P/TiO_2@NC with hollow mesoporous structure can establish a favorable three-phase interface and shorten the electronic/mass transport path to accelerate reaction kinetics. Consequently, Cu_3P/TiO_2@NC indicated robust electrocatalytic activity in alkaline medium compared to single-component catalysts and benchmark Pt/C. Cu_3P/TiO_2@NC exhibits a greater power density of 182.9 mW cm^{-2} and excellent cyclability over 220 h than Pt/C + RuO_2 in Zn-air battery. The flexible properties endow Cu_3P/TiO_2@NC with promising application prospects in wearable electronic devices. This work may provide an avenue to construct hollow-porous-structured catalysts with synergistic effects for renewable energy devices.

1. Introduction

Increasing environmental issues and fossil fuel depletion have inspired the advancement of sustainable and renewable energy conversion devices [1,2]. Fuel cells, metal-air batteries, and metal-ion batteries were promising next-generation energy devices due to their high efficiency and low CO_2 footprints [3]. Thereinto, in response to the feature of portable and wearable flexible electronic devices [4]. Zn-air batteries (ZAB) possesses the peculiarities of cost-effectiveness, extraordinary theoretical energy density (1086 Wh kg^{-1}), eco-friendliness, and intrinsic safety, which are demanded features of the next-generation sustainable flexible energy equipment [5–7]. Nevertheless, the bottleneck of ZAB's development stems from the sluggish kinetics of the oxygen reduction reaction (ORR) owing to its intricate multielectron transfer pathway occurring at the three-phase interface [8]. Although Pt-based materials were considered preeminent electrocatalysts, their extensive applications were inevitably plagued by high cost, scarcity, and insufficient durability [9,10]. Accordingly, putting more efforts into exploring active catalysts highly to vanquish the sluggish kinetics of ORR was critical for the pervasive application of ZAB.

A promising ORR electrocatalyst was generally dominated by the strong synergy between the metal and support and the porous structure in favor of electron/mass transport [11,12]. In this regard, porous carbon support can provide visible superiority because of its momentous conductivity and high specific surface area [13]. Particularly, pyridine N was considered the most favorable bonding mode for ORR in the existence of doped nitrogen [14]. Alternatively, transition metal oxides (TMO) have attracted interest as supports because of strong metal-support interactions (SMSI) between matrix and metal [15]. Previous studies have found that the strong SMSI of TiO_2 originates from electronic interactions that accelerate the electron transfer [16,17]. Meanwhile, the rational combination of TiO_2 and N-doped carbon materials can availably expand its electrical conductivity and thus enhance ORR performance [18]. Moreover, some reports indicated that the electronic structure of TMO supports was impacted by introducing

* Corresponding authors.
E-mail addresses: isimjant@sabic.com (T.T. Isimjan), xlyang@gxnu.edu.cn (X. Yang).
[1] These authors contributed equally.

https://doi.org/10.1016/j.apcatb.2022.121991
Received 20 March 2022; Received in revised form 24 August 2022; Accepted 13 September 2022
Available online 14 September 2022

transition metals [19–21]. The low conductivity and particles agglomeration features of transition metal phosphides (TMPs) with metalloid characteristics, such as Cu_3P, impede its application in electrocatalysis. However, charge transfer was induced by loading Cu_3P onto TMO support. Additionally, the encapsulation of carbonaceous material can resist agglomeration to enhance durability. The electrocatalyst was thus endowed with quick reaction kinetics. Combined with the above factors, we reported an innovative Cu_3P/TiO_2 hybrid catalyst anchored on the 3D hollow mesoporous N-doped carbon nanospheres by high-temperature treatment. The electronic interaction between Ti and P species was induced by innovating Cu_3P. DFT calculations indicated that electron interaction between Cu_3P and TiO_2 can stimulate charge transfer and reduce free energies of oxygen-containing intermediate, endowing catalyst fast ORR kinetics. Moreover, the N, C co-doped matrix helps to overcome the low conductivity of TiO_2. The unordinary hollow mesoporous structure constructs a suitable three-phase interface synchronously provides a larger specific surface area, contributing to reduce diffusion resistance and expose a high density of active sites. Consequently, the optimized catalyst displays excellent ORR activity in alkaline electrolyte, outperforming the benchmark Pt/C and monometallic materials. Notably, the Cu_3P/TiO_2@NC-based ZAB exhibits a high peak power density of 182.9 mW cm^{-2} and outstanding durability for 220 h, confirming its promising application in energy conversion devices.

2. Experimental procedures

2.1. Chemicals

Ammonium hydrogen difluoride (98 %), ethanol, ammonia solution (25–28 %), 1-Hexadecylamine (HAD, 90%), Copper (II) acetate monohydrate ($Cu(Ac)_2{\cdot}H_2O$), analytic grade), melamine, red phosphorus (P) and Titanium isopropoxide (TIP, 95 %). Nafion solution (5 wt%) and Pt/C (20 wt%) were obtained from Alfa Aesar. The Milli-Q ultrapure water with a resistance of 18.2 MΩ·cm was used in the experiment. All chemicals were used without further purification.

2.2. Synthesis of SiO_2@RF

The SiO_2@RF was prepared by stirring reaction under room temperature according to our previous work [22].

2.3. Synthesis of TiO_2@NC

The TiO_2 @NC was prepared according to the reported work with slightly modification [23]. In a typical procedure, 360 mg SiO_2@RF and 320 mg HAD was dissolved in a mixture of 0.8 mL of ammonia solution and 31.0 mL of ethanol. After ultrasonic treatment for 30 min, 0.4 mL of TIP was fleetly dropped into the above solution with successive agitating for 2 h at room temperature. The precipitates were centrifuged and washed with ethanol several times to eliminate superfluous organic species and dried in oven 60 ℃. Subsequently, the obtained product was uniformly ground with melamine (mass ratio=1:5) and annealed at 700 ℃ for 3 h under N_2 atmosphere with a heating rate of 5 ℃/min. The SiO_2 core was etched by 1 M ammonium hydrogen difluoride solution for 12 h to obtain TiO_2@NC.

2.4. Synthesis of Cu_3P/TiO_2@NC

A certain amount of TiO_2@NC, 50 mg $Cu(Ac)_2{\cdot}H_2O$ and x mg P (x = 50, 100, 200) were ground uniformly and calcined at T °C (T = 800, 900, 1000) for 2 h under N_2 atmosphere. the Cu_3P/TiO_2@NC refers to that product obtained at a temperature of 900 ℃ and P of 100 mg unless stated otherwise.

As a control, the Cu_3P@C was prepared by using the same protocol except that carbon black was regarded as the support.

3. Results and discussion

3.1. Synthesis and characterization of catalysts

As depicted in Scheme 1, the Cu_3P/TiO_2@NC was obtained by a facile high-temperature phosphating process to load the Cu_3P species on the TiO_2@NC hollow nanospheres. Specifically, SiO_2@RF nanospheres were synthesized via a phenolic reaction to coat carbonaceous substances on the surface of SiO_2. After that, HDA and SiO_2@RF nanospheres were uniformly dispersed in a mixed solution so that HDA surfactants was segregated to the surface of the nanospheres. TIP was subsequently added to the above solution under stirring. The amino groups of HDA interact with the TIP hydrolysate to form a composite material coated with the nanospheres [24]. The X-ray diffraction (XRD) pattern of TiO_2@NC was obtained by removing the SiO_2 core, and it somewhat displays the characteristic diffraction peaks of monoclinic TiO_2 (JCPDS: 46–1238 and 48–1278), confirming the TiO_2 loading onto the template (Fig. S1) [25]. Transmission electron microscope (TEM) and scanning electron microscope (SEM) indicated that TiO_2@NC exhibits a hollow structure (Figs. S2a-b). Furthermore, the homogeneous dispersion of C, N, O and Ti on the entire nanosphere was confirmed by elemental mappings (Fig. S2c). Afterwards, Cu ions were loaded on the TiO_2@NC nanospheres during the high-temperature phosphating. The Cu ions amount was up to 35.86 wt%, as corroborated by inductively coupled plasma mass spectroscopy (ICP-MS) (Table S1). Of note, red P was considered an environment-friendly phosphorus source owing to not engender toxic gases at high-temperature process.

The crystal phases of the resultant catalysts were authenticated by XRD patterns (Fig. 1a). The primary peaks were matched well with hexagonal Cu_3P (JCPDS: 02–1263) and tetragonal TiO_2 (JCPDS: 21–1276) [22,25], indicating the formation of Cu_3P with high phase-purity and crystallinity in the TiO_2@NC support. Notably, the crystal structure of TiO_2 transforms from monoclinic to tetragonal crystal phase owing to the temperature increment [26]. The morphology and microstructure of Cu_3P/TiO_2@NC was revealed by SEM and TEM. The Cu_3P/TiO_2@NC took on a hollow structure similar to TiO_2@NC, confirming that the support structure was not destroyed after loading Cu_3P (Fig. 1b-c and Fig. S3). Generally, the hollow structure was promising to expedite the mass and electron transfer during the reaction [27,28]. The high-resolution TEM (HR-TEM) image and the corresponding lattice spacing profiles were presented in Fig. 1d. The lattice strips with spacings of 0.248 and 0.201 nm in the red region can be retrieved to the (300) plane of Cu_3P and the (101) plane of TiO_2, respectively [29]. The subtle distortion region can be sharply observed in the HR-TEM image of Cu_3P/TiO_2@NC, which was attributed to the contact between the Cu_3P and TiO_2 particles (Fig. S4) [30]. Simultaneously, the hollow structure of Cu_3P/TiO_2@NC was further unveiled by high-angle annular dark-field scanning transmission electron microscopy (HAADF-STEM) in Fig. 1e. The corresponding element mappings elucidated the uniform distribution of C, O, P, N, Cu and Ti elements in the nanosphere (Fig. 1f). Besides, ICP-MS and element mapping confirmed that the weak lattice fringes of TiO_2 in the HR-TEM image was attributed to the low content of Ti in Cu_3P/TiO_2@NC. As expected, the above results confirmed that Cu_3P was successfully incorporated into the TiO_2@NC support.

The Raman spectra of all catalysts were plotted in Fig. 2a. Generally, D- and G-band reflect the disorder or edge defects and graphitization degree of carbon species, respectively [31,32]. The intensity ratio (I_D/I_G) of the D- and G-band of Cu_3P/TiO_2@NC (1.39) was higher than that of Cu_3P@C (1.28) and TiO_2@NC (1.10), confirming that the catalyst harvests more edge defects after loading Cu_3P [33,34]. As a result, it is conducive to improve the electrocatalytic activity of Cu_3P/TiO_2@NC.

The N_2 adsorption/desorption isotherm manifests the Ⅳ-type curves with palpable hysteresis loop that confirmed the mesoporosity of Cu_3P/TiO_2@NC nanospheres [35]. The generation of mesopores may be attributed to the elimination of SiO_2 core. Meanwhile, the

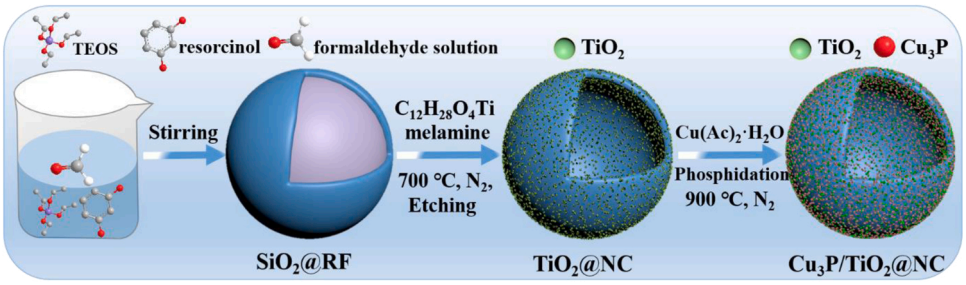

Scheme 1. Schematic diagram of the synthesis of Cu_3P/TiO_2@NC.

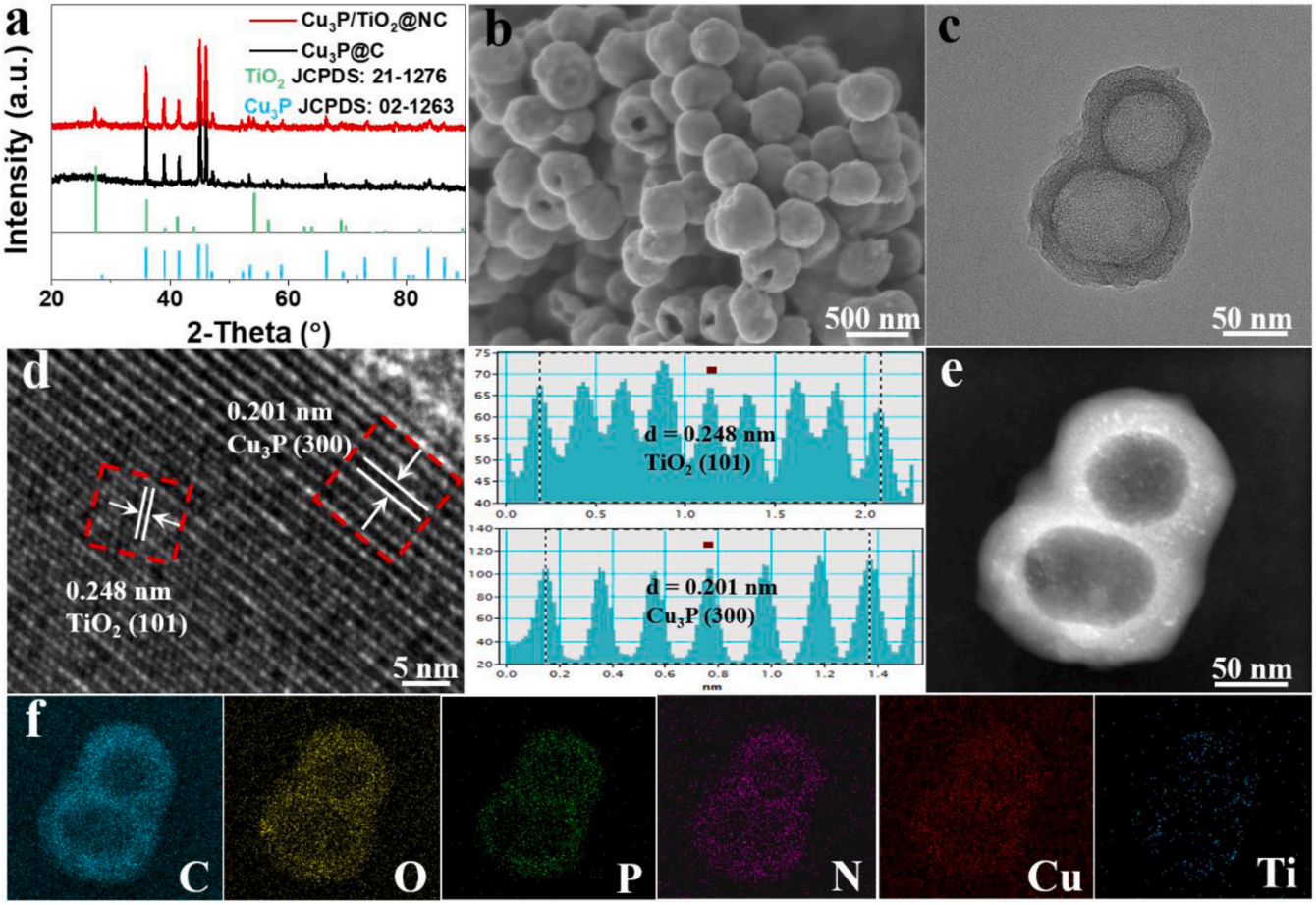

Fig. 1. (a) XRD patterns of Cu_3P/TiO_2@NC and Cu_3P@C. (b) SEM, (c) TEM, (d) HR-TEM and the corresponding lattice spacing profiles of the dotted line regions, (e) HAADF-STEM images and (f) elemental mappings of Cu_3P/TiO_2 @NC.

Brunauer-Emmett-Teller (BET) surface area of Cu_3P/TiO_2@NC was calculated to be 196.3 $m^2\ g^{-1}$ (Fig. 2b), which was conducive to increase the attainability of active sites [36]. The active catalyst nanoparticles were located on the inner and outer surfaces of shell owing to unique hollow mesoporous structure. Moreover, the mesoporous network connecting the interior and exterior provide channels for reactant molecules diffusion into the active site. The mesoporous structure was further affirmed by pore-size distribution (≈ 5.3 nm, inset in Fig. 2b), which favored adsorption of O_2 molecule and transport of electrons and mass at the three-phase interface and exhibited enhanced ORR activity [34,37]. As depicted in Fig. 2c and S5, Cu_3P/TiO_2@NC (121.1°) has a smaller contact angle compared to Cu_3P/C (129.3°) and TiO_2@NC (131.8°), elucidating that Cu_3P/TiO_2@NC possesses higher hydrophilicity. Hydrophilicity can be explained according to the equation: $h = 2\sigma\cos\theta/(\rho g r)$ [38]. The liquid height (h) is proportional to the capillary radius (r). Therefore, the Cu_3P/TiO_2@NC with hollow mesoporous structure can provide a more potent capillary force to facilitate electrolyte diffuse, promoting the contact between active sites with reactants and accelerating ORR kinetics [39,40].

The surface composition and chemical environment of catalysts were further investigated by X-ray photoelectron spectroscopy (XPS). The survey spectra manifest the co-existence of Cu, Ti, C, O, N and P elements in the as-prepared materials, which was coincident with mapping analysis (Fig. S6a). As depicted in Figs. S6b-d, the high-resolution C 1 *s* spectra of as-prepared catalysts were deconvoluted into four peaks as C═C (284.0 eV), C-C (284.8 eV), C-O/C-N (285.8 eV), O-C═O (288.0 eV) [41]. Pyridinic-N (397.8 eV), pyrrolic-N (399.2 eV) and graphitic-N (400.6 eV) were displayed in the high-resolution N 1*s* spectra (Figs. S6e-f) [42]. Among them, pyridinic-N and graphitic-N can modulate the charge redistribution to enhance the ORR catalytic activity

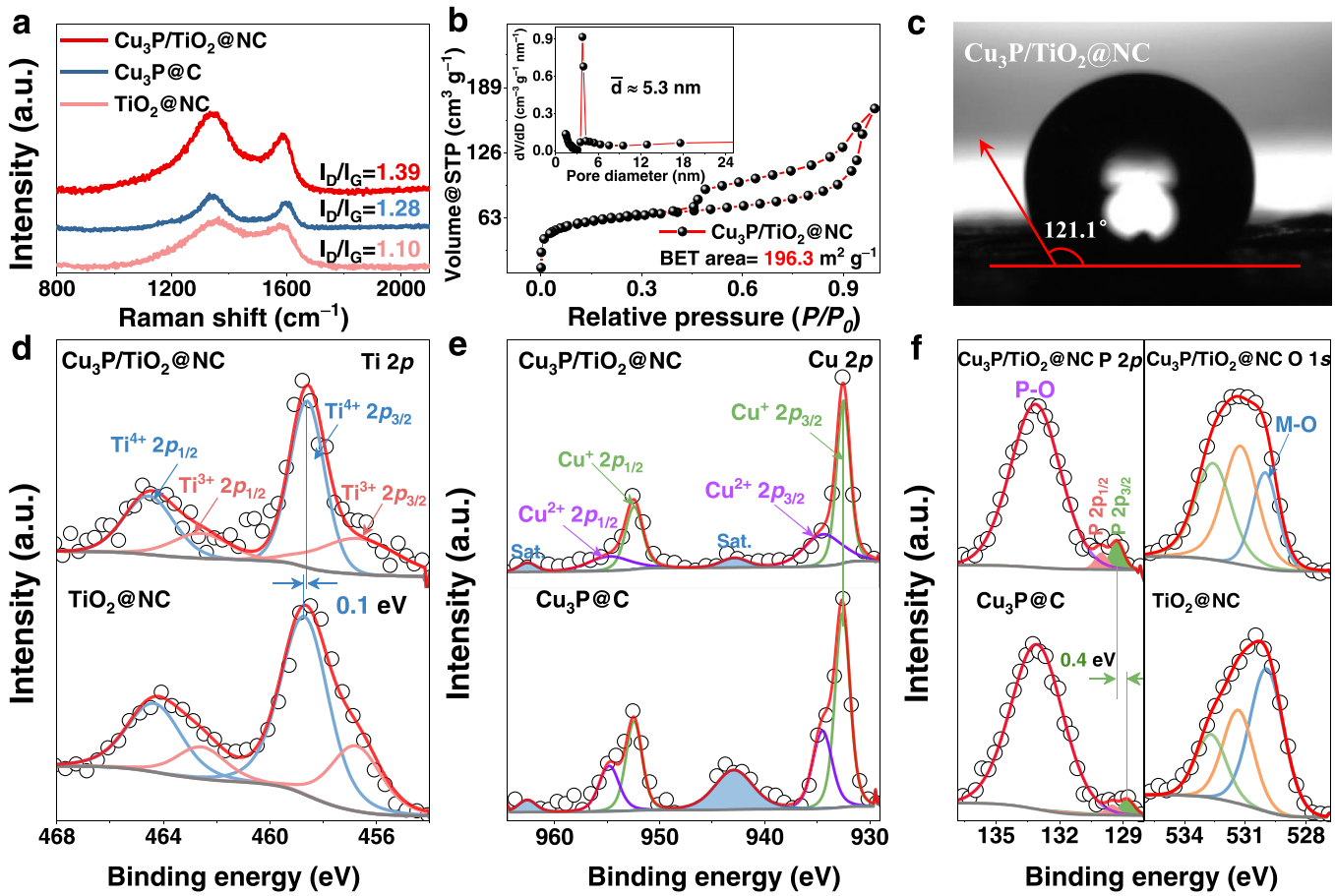

Fig. 2. (a) Raman spectra of the different catalysts. (b) N_2 adsorption/desorption isotherms and corresponding pore size distribution for Cu_3P/TiO_2@NC (inset). (c) Bubble contact angle image of Cu_3P/TiO_2@NC. High-resolution XPS spectra of (d) Ti 2*p*, (e) Cu 2*p*, and (f) P 2*p* and O 1*s* regions in Cu_3P/TiO_2@NC, Cu_3P@C, and TiO_2@NC, respectively.

[43]. The Ti 2*p* spectrum of Cu_3P/TiO_2@NC indicates two peaks at 458.6 and 464.5 eV were assigned to $2p_{3/2}$ and $2p_{1/2}$ of Ti^{4+} in TiO_2 [44]. The doublet peaks of Ti^{3+} appear 456.7 and 462.6 eV, indicating the partial reduction of Ti^{4+} by carbon at high temperature [45]. The binding energies of Ti^{4+} are 0.1 eV lower than that of TiO_2@NC (Fig. 2d). Furthermore, in the Cu 2*p* region of Cu_3P/TiO_2@NC and TiO_2@NC (Fig. 2e), the peaks at 932.5 and 952.4 eV were indexed to the Cu $2p_{3/2}$ and Cu $2p_{1/2}$ of Cu^+ in Cu_3P, respectively. The binding energies at 934.5 and 954.8 eV were assigned to Cu^{2+}, resulting from surface oxidation upon exposure to the air. Furthermore, the peaks centered at 942.9 and 962.6 eV contributed to satellite peaks [46]. The presence of Cu^+ was further corroborated by auger electron spectroscopy (AES) (Fig. S7). The P 2*p* spectrum was fitted into three peaks at 129.3, 130.0 and 133.1 eV corresponding to $2p_{3/2}$ and $2p_{1/2}$ of Cu-P and P-O bonds [47]. The presence of P-O bonds was attributed to the surface oxidation of phosphide. Meanwhile, the O 1*s* spectra emerge three palpable peaks at 530.0, 531.3 and 532.6 eV can be attributed M-O, C-O and adsorbed OH groups, respectively (Fig. 2f) [48,49]. Interestingly, the binding energies of Cu-P display positive shifted by 0.4 eV compared with Cu_3P@C. The shift of Ti^{4+} and Cu-P in the binding energy demonstrates the charge transfer from P to Ti species, revealing that the introduction of Cu_3P promotes strong electronic interactions [50]. Notably, the interaction, engendered by charge redistribution, give rise to faster charge/mass transfer and enhance ORR activity [51]. As expected, XPS analysis verified that the successful preparation of Cu_3P and TiO_2, which is identical with the XRD and HR-TEM results.

3.2. Electrocatalytic ORR activity of materials

The electrocatalytic ORR performance of as-prepared materials was estimated in 0.1 M KOH solution. The optimal catalyst, noted as Cu_3P/TiO_2@NC, was obtained when the mass ratio of red P to precursor was 2/1 and the calcination temperature was 900 °C during a series of optimization (Figs. S8 and S9). As displayed in Fig. S10, the cyclic voltammetry (CV) curves of all catalysts exhibited distinct reduction peaks in O_2-saturated electrolytes compared to N_2-saturated ones, confirming the selectivity of the catalysts for oxygen reduction. Furthermore, the anodic/cathode peaks at 0.90 and 0.61 V were assigned to the redox reactions of Cu species [52]. Moreover, Cu_3P/TiO_2@NC, Cu_3P@C and TiO_2@NC exhibited poor OER performance (Fig. S11).

Linear sweep voltammetry (LSV) curves of Cu_3P/TiO_2 @NC manifest an onset potential (E_{onset}) of 0.95 V and a half-wave potential ($E_{1/2}$) of 0.80 V, which were substantially superior to those of Cu_3P@C (0.80 V, 0.63 V), TiO_2@NC (0.90 V, 0.74 V) and most recently reported transition metal-based electrocatalysts (Table S2), whereas slightly lower than Pt/C (1.01 V, 0.85 V) (Fig. 3a). The above results illustrated that Cu_3P/TiO_2@NC bears favorable ORR activity, which attributed to the strong electronic interaction induced by introducing Cu_3P and the hollow mesoporous structure critical to expose more active sites. Notably, TiO_2 was regarded as the main active center. Cu_3P plays an auxiliary role. Moreover, the kinetic density (J_k) of Cu_3P/TiO_2@NC is as high as 4.95 mA cm^{-2} at 0.8 V in contrast to Cu_3P@C (0.14 mA cm^{-2}) and TiO_2 @NC (0.95 mA cm^{-2}), explicating that Cu_3P/TiO_2@NC possessed faster kinetics (Fig. 3b) [53]. The mass activity of Cu_3P/TiO_2 @NC was up to 6.43 mA mg^{-1} at 0.8 V, which was 35.7 and 5.2 times higher than that

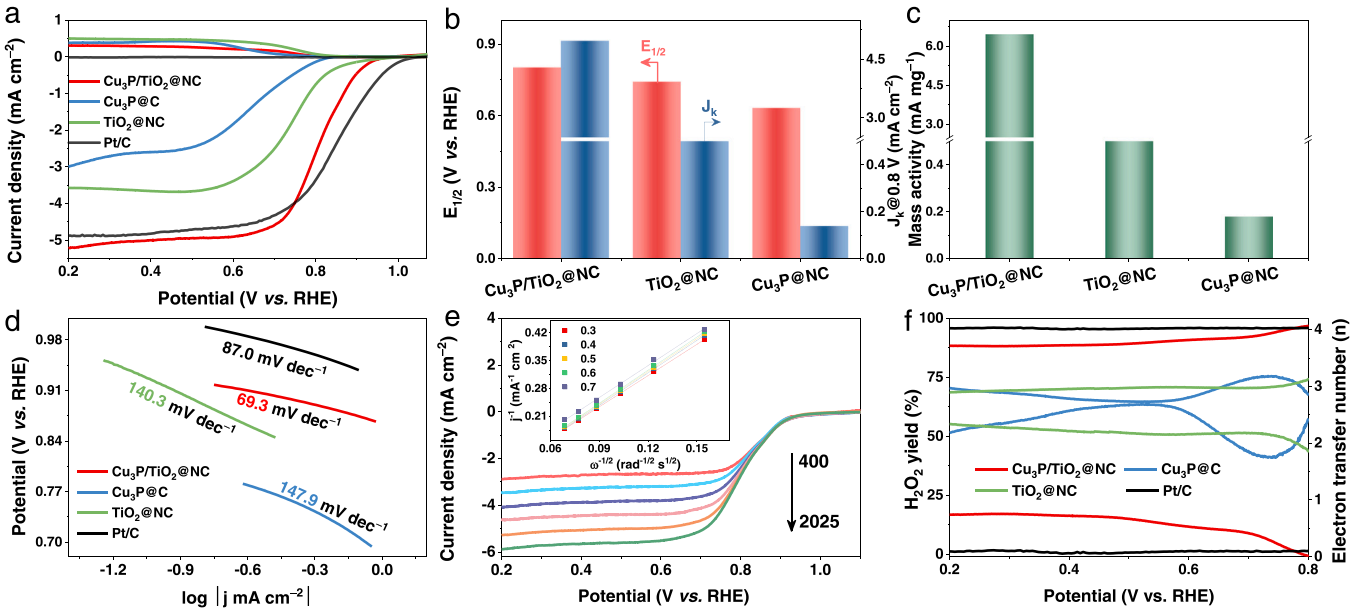

Fig. 3. Electrocatalytic ORR performances of the catalysts in 0.1 M KOH solutions. (a) LSV curves, (b) summary of the corresponding $E_{1/2}$ and J_k (E = 0.8 V) values, and (c) mass activity (E = 0.8 V) of the as-prepared catalysts and Pt/C. (d) Tafel plots. (e) Polarization curves of Cu_3P/TiO_2 @NC at various rotating speeds from 400 to 2025 rpm and the corresponding K-L plots (inset). (f) H_2O_2 yield (%) and electron transfer number (n) from various catalysts.

of Cu_3P@C (0.18 mA mg^{-1}) and TiO_2 @NC (1.23 mA mg^{-1}), respectively, certifying that its great potential for practical applications (Fig. 3c) [54]. As shown in Fig. 3d, Cu_3P/TiO_2 @NC exhibited the lowest Tafel slope value of 69.3 mV dec^{-1} being beyond Cu_3P@C (147.9 mV dec^{-1}), TiO_2@NC (140.3 mV dec^{-1}) and benchmark Pt/C (87.0 mV dec^{-1}), suggesting more advantageous kinetics during ORR.

The reaction mechanism of Cu_3P/TiO_2@NC was elucidated by rotating disk electrode (RDE) technique. As illustrated in Fig. 3e, the Koutecky–Levich (K–L) plot with good linearity was obtained by recording LSV curves at various rotation speeds. This was accordance with the first-order reaction kinetics of ORR [55]. The electron transfer number (n) was calculated to be about 3.5 according to the K-L equation, signifying that ORR process follows a four-electron transfer pathway. The rotating ring-disk electrode (RRDE) technique was executed to further interrogate the reaction mechanism. The value of n was evaluated to be ~3.7 (Fig. 3f), which is consistent with the RDE analysis. Simultaneously, the H_2O_2 yield of Cu_3P/TiO_2@NC (< 20 %) visibly lower than that of Cu_3P@C and TiO_2@NC, exemplifying that the electronic interaction of TiO_2 induced by Cu_3P has an indispensable effect on the selectivity of product.

To further probe the intrinsic activity of electrocatalyst. The electrochemically active surface area (ECSA) was discussed by calculating

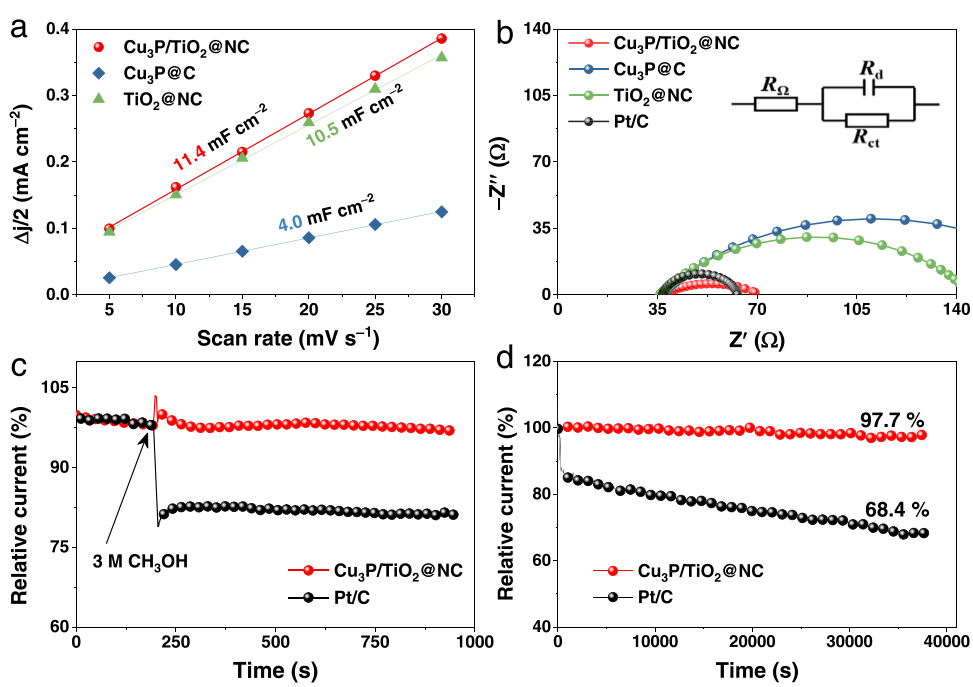

Fig. 4. (a) C_{dl} values (b) Nyquist plots of the impedance for the catalysts and the corresponding equivalent circuit (inset). (c) Methanol tolerance tests and (d) Chronoamperometric response of Cu_3P/TiO_2 @NC and Pt/C.

the value of the electric double-layer capacitance (C_{dl}) [56]. C_{dl} was obtained based on CV curves at various scan rates from 5 to 30 mV s^{-1} (Fig. S12). The Cu_3P/TiO_2@NC arises a C_{dl} value of 11.4 mF cm^{-2}, outperforming those of Cu_3P@C (4.0 mF cm^{-2}) and TiO_2@NC (10.5 mF cm^{-2}), meaning that Cu_3P/TiO_2@NC can expose more active sites to contact with reactants and boost ORR performance (Fig. 4a). The above results can be attributed to the large specific surface area of Cu_3P/TiO_2@NC with a hollow mesoporous structure. Electrochemical impedance spectroscopy (EIS) certified that Cu_3P/TiO_2@NC possesses comparatively small charge transfer resistance (Fig. 4b), attesting the heightened ORR kinetics by introducing Cu_3P. The stability and methanol tolerance were essential parameters for evaluating catalysts. As presented in Fig. 4c, the current of Cu_3P/TiO_2@NC undergoes a tiny drop compared to Pt/C after the addition of methanol at approximately 200 s. In addition, the robust stability of Cu_3P/TiO_2@NC was testified by current retention of 97.7% after the chronoamperometric response of 40000 s (Fig. 4d). The above results signify that Cu_3P/TiO_2@NC possesses admirable methanol tolerance and stability than that of Pt/C, meaning it has potential practical application prospects in direct methanol fuel cells and metal-air battery.

3.3. DFT calculation

DFT calculations were performed to elucidate the influence of leading into Cu_3P in the electronic structure and ORR activity of TiO_2. The optimized structure models of Cu_3P/TiO_2, Cu_3P, and TiO_2 were shown in Fig. S13. The calculated density of states (DOS) and partial density of states (PDOS) of different models were depicted in Fig. 5a and b, respectively. The higher DOS around the Fermi level of Cu_3P/TiO_2 than that of TiO_2 due to the introduction of Cu_3P, which impacted the electronic structures of TiO_2. Consequently, Cu_3P/TiO_2 composites enhance electron transport properties and facilitate adsorption/desorption of oxygen-containing intermediates, thereby improving the conductivity and reducing the reaction energy barriers [57]. As a complement, PODS results illustrated that the *d*-band center values of Cu and Ti (−2.64 and 0.05 eV) in Cu_3P/TiO_2 were more negative relative to those of Cu_3P (−2.29 eV) and TiO_2 (0.87 eV). The lower *d*-band center of Cu and Ti in Cu_3P/TiO_2 was promising to weaken the adsorption of oxygen intermediates, hence accelerating ORR reaction kinetics [58]. In addition, Fig. 5c indicated that the electrons were accumulated in the edge of Cu_3P, whereas the one was depleted around TiO_2. The result suggests the existence of charge synergistic between Cu_3P and TiO_2, which was consistent with the XPS analysis. The Gibbs free energy was a key parameter for annotating the origin of electrocatalytic activity. The corresponding free energy variations of intermediates were calculated based on the stable adsorption configurations (Fig. 5d). As indicated in Fig. S14 and Table S3, all elementary steps were exothermic processes in Cu_3P/TiO_2 and Cu_3P. In contrast, the formation of O* was endothermic in TiO_2 at an equilibrium potential of 0 V. Consequently, at U = 1.23 V, the transition from OOH* to O_2* was rate-determining steps (RDS) in TiO_2 (Fig. 5e). Differently, the OH* intermediate desorption was changed to RDS when the introduction of Cu_3P. Simultaneously, OH* desorption free energy in Cu_3P/TiO_2 (0.07 eV) was lower than that of Cu_3P (1.38 eV), which was propitious for the desorption behavior of OH* in the composites. Excitingly, the overpotential of Cu_3P/TiO_2 was distinctly lower than those of Cu_3P and TiO_2 (Fig. 5f). The above results indicated that the strong interaction between Cu_3P and TiO_2 was conducive to optimizing adsorption of oxygen intermediates and facilitate electron transfer, thus Cu_3P/TiO_2 exhibited the best ORR activity, which was in agreement with the experimental results.

3.4. Performance of Zn-air battery

The Zn-air battery (ZAB) was constructed by applying Cu_3P/TiO_2@NC as air cathode to appraise its feasibility in practice energy storage-conversion equipment (Fig. 6a). Fig. S15a shows that $Cu_3P/$

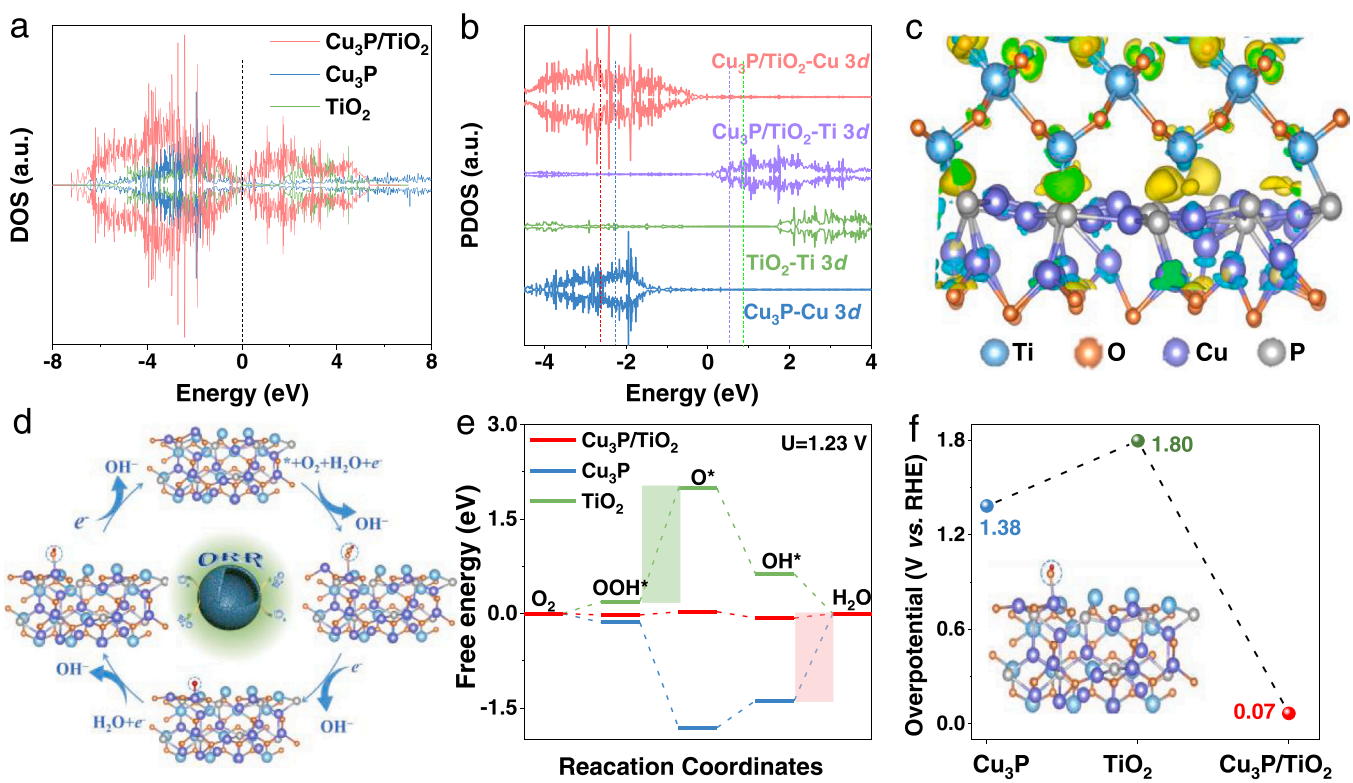

Fig. 5. (a) DOS, (b) PDOS of Ti 3*d* and Cu 3*d* orbitals of different models. (c) The charge density differences of Cu_3P/TiO_2 model. Yellow and green region depict electron accumulation and depletion, respectively. (d) The reaction mechanism of ORR on Cu_3P/TiO_2 model in 0.1 M KOH electrolyte. (e) Free energy diagram of ORR at an equilibrium potential of 1.23 V, and (f) corresponding overpotential (inset: RDS of Cu_3P/TiO_2 configuration) for Cu_3P/TiO_2, Cu_3P, and TiO_2.

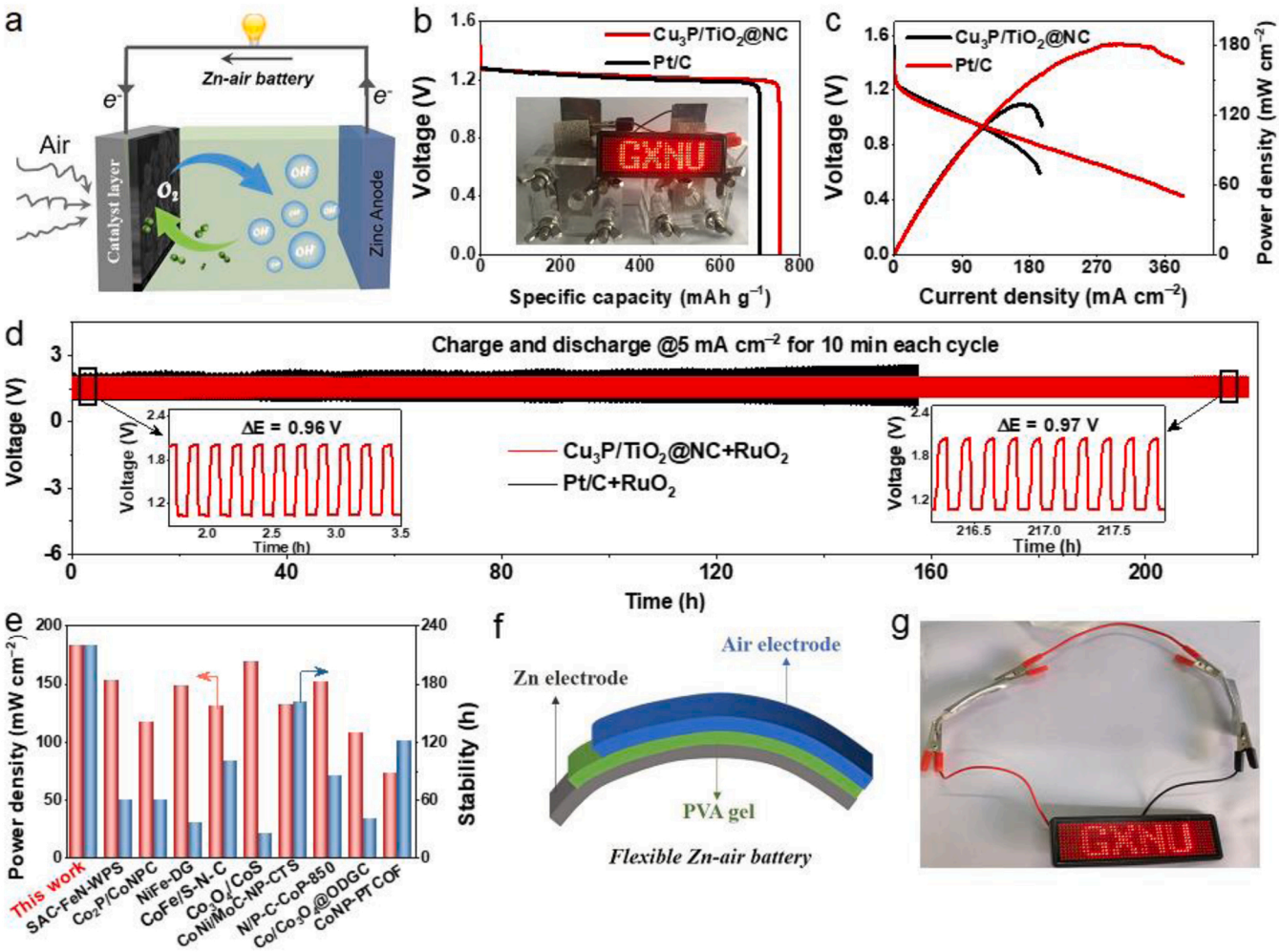

Fig. 6. Application of Cu_3P/TiO_2 @NC in Zn–air batteries. (a) Schematic configuration of the liquid ZAB. (b) Specific capacity plots and digital image of LED panel lit by two ZABs in series(inset). (c) Discharge curves and the corresponding power densities of the catalysts. (d) Long-term cycling stability of liquid ZAB at 5.0 mA cm^{-2}. (e) Power density and stability contrast of Cu_3P/TiO_2 @NC with currently reported transition metal catalysts. (f) Schematic of the all-solid-state flexible ZAB. (g) Photograph of LED panel powered by two solid-state ZABs in series.

TiO_2@NC-based ZAB achieved an open circuit voltage (OCV) of 1.30 V, reasonably lower than that of Pt/C (1.47 V). Additionally, Fig. 6b indicates that ZAB based on Cu_3P/TiO_2@NC delivers a specific capacity (747.3 mAh g_{Zn}^{-1}, 91.1% utilization of the theoretical capacity) larger than that of Pt/C (700.0 mAh g_{Zn}^{-1}, 85.4 %) [59]. As a practical illustration, the LED plate with a voltage of ~ 3 V can be lit by connecting two ZABs in series (inset in Fig. 6b). Fig. 6c shows the polarization curves of ZAB, the peak power density of Cu_3P/TiO_2@NC reaches 182.9 mW cm^{-2}, which is evidently higher than that of Pt/C (129.4 mW cm^{-2}). Furthermore, the discharge curves of the Cu_3P/TiO_2@NC-based ZAB at various current densities declared that the voltage retention was 99% when the current density was recovered to 2 mA cm^{-2}, acknowledging its good rate capability (Fig. S15b).

The durability of ZAB was evaluated by charge-discharge cycling testing at a galvanostatic current of 5 mA cm^{-2}. The Cu_3P/TiO_2@NC+RuO_2-based ZAB exhibits superior stability with almost negligible attenuation of the discharge-charge voltage gap after 220 h of continuous operation. In contrast, the Pt/C+RuO_2-based ZAB exhibits a conspicuous decay after 160 h, which further elaborates the distinguished ORR stability of Cu_3P/TiO_2@NC (Fig. 6d). Fig. 6e indicates that the power density and stability of ZAB assembled with Cu_3P/TiO_2@NC as an air cathode is also comparable among recently reported most catalysts. The schematic diagram and photographs of the flexible ZAB were depicted in Fig. 6f and Fig. S16. Interestingly, two flexible ZABs connected in series can successfully power a LED plate (Fig. 6 g). As expected, Cu_3P/TiO_2@NC possesses promising applications in energy conversion devices.

Taken together, Cu_3P/TiO_2 @NC exhibits robust ORR activity and stability compared to Cu_3P@C, TiO_2@NC, and Pt/C due to its distinctive structural superiority: (i) The hollow mesoporous structure of Cu_3P/TiO_2 @NC provide a good three-phase contact interface and shortens ion transport paths to expedite ORR kinetics [60]. (ii) The large specific surface area of Cu_3P/TiO_2 @NC with hollow mesoporous structure can expose more active sites. (iii) The strong synergistic effect between Cu_3P and TiO_2 species can modulate electronic structure resulting in faster electronic/mass transport and fast reaction kinetics [61]. Furthermore, the hollow structure with larger empty space was favorable for storing charges, which enables Cu_3P/TiO_2 @NC to exhibit superb cyclical stability in practical applications [51].

4. Conclusions

To summarize, we have affirmed a strategy to induce charge transfer feature of composites by doping Cu_3P at high temperature. The optimized Cu_3P/TiO_2@NC catalyst exhibits excellent ORR activity with a half-wave potential of 0.80 V, outperforming the benchmark Pt/C and recently reported transition metal-based catalysts. XPS and DFT calculation indicated that the superior ORR performance originates from the

strong synergistic effect between Cu_3P and TiO_2 species. Furthermore, BET and contact angle tests confirmed that a high specific surface area of Cu_3P/TiO_2@NC with mesoporous structure can construct an available three-phase interface and exposes a high density of active sites, which was advantageous for electron/mass transport and accelerate the reaction kinetics. As a consequence, Cu_3P/TiO_2@NC was adopted as the cathode catalyst for ZAB. The peak power density could reach 182.9 mW cm^{-2} as well as superior stability with no distinct current decay after continuous charge-discharge for 220 h, outperforming to Pt/C + RuO_2. The above results confirmed that Cu_3P/TiO_2 @NC possesses promising applications in metal-air batteries.

CRediT authorship contribution statement

Man Guo: Methodology, Writing - original draft. **Zhiyang Huang:** Investigation and methodology. **Yuan Qu:** Data curation. **Lixia Wang:** Investigation. **Huatong Li:** Data curation, Methodology. **Tayirjan Taylor Isimjan:** Writing-review & editing. **Xiulin Yang:** Supervision, Writing-review & editing.

Declaration of Competing Interest

The authors declare that they have no known competing financial interests or personal relationships that could have appeared to influence the work reported in this paper.

Data availability

The data that has been used is confidential.

Acknowledgments

This work has been supported by the National Natural Science Foundation of China (no. 21965005), Natural Science Foundation of Guangxi Province (2018GXNSFAA294077, 2021GXNSFAA076001), Project of High-Level Talents of Guangxi (F-KA18015), and Guangxi Technology Base and Talent Subject (GUIKE AD18126001, GUIKE AD20297039).

Appendix A. Supporting information

Supplementary data associated with this article can be found in the online version at doi:10.1016/j.apcatb.2022.121991.

References

[1] S. Ramakrishnan, D.B. Velusamy, S. Sengodan, G. Nagaraju, D.H. Kim, A.R. Kim, D. J. Yoo, Rational design of multifunctional electrocatalyst: an approach towards efficient overall water splitting and rechargeable flexible solid-state zinc–air battery, Appl. Catal. B: Environ. 300 (2022), 120752, https://doi.org/10.1016/j.apcatb.2021.120752.

[2] D. Zheng, W. Liu, X. Dai, J. Feng, X. Xu, R. Yin, W. Que, W. Shi, F. Wu, H. Wu, X. Cao, Compressible Zn–Air batteries based on metal–organic frameworks nanoflake-assembled carbon frameworks for portable motion and temperature monitors, Adv. Energy Sustain. Res. 3 (2022), 2200014, https://doi.org/10.1002/aesr.202200014.

[3] N. Logeshwaran, S. Ramakrishnan, S.S. Chandrasekaran, M. Vinothkannan, A. R. Kim, S. Sengodan, D.B. Velusamy, P. Varadhan, J.-H. He, D.J. Yoo, An efficient and durable trifunctional electrocatalyst for zinc–air batteries driven overall water splitting, Appl. Catal. B: Environ. 297 (2021), 120405, https://doi.org/10.1016/j.apcatb.2021.120405.

[4] M. Zhao, H. Liu, H. Zhang, W. Chen, H. Sun, Z. Wang, B. Zhang, L. Song, Y. Yang, C. Ma, Y. Han, W. Huang, A. pH-universal, ORR catalyst with single-atom iron sites derived from a double-layer MOF for superior flexible quasi-solid-state rechargeable Zn–air batteries, Energy Environ. Sci. 14 (2021) 6455–6463, https://doi.org/10.1039/D1EE01602D.

[5] T. Cui, Y.-P. Wang, T. Ye, J. Wu, Z. Chen, J. Li, Y. Lei, D. Wang, Y. Li, Engineering dual single-atom sites on 2D ultrathin N-doped carbon nanosheets attaining ultra-low temperature Zn-air battery, Angew. Chem. Int. Ed. 61 (2022), e202115219, https://doi.org/10.1002/anie.202115219.

[6] R. Ren, G. Liu, J.Y. Kim, R.E.A. Ardhi, M.X. Tran, W. Yang, J.K. Lee, Photoactive g-C_3N_4/CuZIF-67 bifunctional electrocatalyst with staggered p-n heterojunction for rechargeable Zn-air batteries, Appl. Catal. B: Environ. 306 (2022), 121096, https://doi.org/10.1016/j.apcatb.2022.121096.

[7] J.-N. Liu, C.-X. Zhao, D. Ren, J. Wang, R. Zhang, S.-H. Wang, C. Zhao, B.-Q. Li, Q. Zhang, Preconstructing asymmetric interface in air cathodes for high-performance rechargeable Zn–Air batteries, Adv. Mater. 34 (2022), 2109407, https://doi.org/10.1002/adma.202109407.

[8] Y. Chen, H. Yao, F. Kong, H. Tian, G. Meng, S. Wang, X. Mao, X. Cui, X. Hou, J. Shi, V_2C MXene synergistically coupling FeNi LDH nanosheets for boosting oxygen evolution reaction, Appl. Catal. B: Environ. 297 (2021), 120474, https://doi.org/10.1016/j.apcatb.2021.120474.

[9] S. Wang, H. Wang, C. Huang, P. Ye, X. Luo, J. Ning, Y. Zhong, Y. Hu, Trifunctional electrocatalyst of N-doped graphitic carbon nanosheets encapsulated with CoFe alloy nanocrystals: the key roles of bimetal components and high-content graphitic-N, Appl. Catal. B: Environ. 298 (2021), 120512, https://doi.org/10.1016/j.apcatb.2021.120512.

[10] W. Liu, D. Zheng, L. Zhang, R. Yin, X. Xu, W. Shi, F. Wu, X. Cao, X. Lu, Bioinspired interfacial engineering of a $CoSe_2$ decorated carbon framework cathode towards temperature-tolerant and flexible Zn–air batteries, Nanoscale 13 (2021) 3019–3026, https://doi.org/10.1039/D0NR08365H.

[11] T. Lu, X. Hu, J. He, R. Li, J. Gao, Q. Lv, Z. Yang, S. Cui, C. Huang, Aqueous/solid state Zn-air batteries based on N doped graphdiyne as efficient metal-free bifunctional catalyst, Nano Energy 85 (2021), 106024, https://doi.org/10.1016/j.nanoen.2021.106024.

[12] H. Feng, C. Zhang, Z. Liu, J. Sang, S. Xue, P.K. Chu, A light-activated TiO_2@In_2Se_3@Ag_3PO_4 cathode for high-performance Zn-Air batteries, Chem. Eng. J. 434 (2022), 134650, https://doi.org/10.1016/j.cej.2022.134650.

[13] J. Li, H. Zhou, H. Zhuo, Z. Wei, G. Zhuang, X. Zhong, S. Deng, X. Li, J. Wang, Oxygen vacancies on TiO_2 promoted the activity and stability of supported Pd nanoparticles for the oxygen reduction reaction, J. Mater. Chem. A 6 (2018) 2264–2272, https://doi.org/10.1039/C7TA09831F.

[14] Q. Li, Y. Chen, F. Du, X. Cui, L. Dai, Bias-free synthesis of hydrogen peroxide from photo-driven oxygen reduction reaction using N-doped γ-graphyne catalyst, Appl. Catal. B: Environ. 304 (2022), 120959, https://doi.org/10.1016/j.apcatb.2021.120959.

[15] Y. Yu, S. You, J. Du, P. Zhang, Y. Dai, M. Liu, B. Jiang, N. Ren, J. Zou, Ti^{3+}-self-doped TiO_2 with multiple crystal-phases anchored on acid-pickled ZIF-67-derived Co_3O_4@N-doped graphitized-carbon as a durable catalyst for oxygen reduction in alkaline and acid media, Chem. Eng. J. 403 (2021), 126441, https://doi.org/10.1016/j.cej.2020.126441.

[16] R. Long, K. Mao, M. Gong, S. Zhou, J. Hu, M. Zhi, Y. You, S. Bai, J. Jiang, Q. Zhang, X. Wu, Y. Xiong, Tunable oxygen activation for catalytic organic oxidation: Schottky junction versus plasmonic effects, Angew. Chem. Int. Ed. 53 (2014) 3205–3209, https://doi.org/10.1002/anie.201309660.

[17] J. Wang, M. Xu, J. Zhao, H. Fang, Q. Huang, W. Xiao, T. Li, D. Wang, Anchoring ultrafine Pt electrocatalysts on TiO_2-C via photochemical strategy to enhance the stability and efficiency for oxygen reduction reaction, Appl. Catal. B: Environ. 237 (2018) 228–236, https://doi.org/10.1016/j.apcatb.2018.05.085.

[18] Q. Han, C. Wu, H. Jiao, R. Xu, Y. Wang, J. Xie, Q. Guo, J. Tang, Rational design of high-concentration Ti^{3+} in porous carbon-doped TiO_2 nanosheets for efficient photocatalytic ammonia synthesis, Adv. Mater. 33 (2021), 2008180, https://doi.org/10.1002/adma.202008180.

[19] X. Lu, Y. Wang, J. Huang, N. Han, H. Li, Z. Yang, Y. Peng, X. Zhang, C. Xu, Boosting the electrochemical nitrogen reduction by rhenium-doping modulated TiO_2 nanofibers, Chem. Eng. J. 434 (2022), 134648, https://doi.org/10.1016/j.cej.2022.134648.

[20] X. Wang, J. Yang, M. Salla, S. Xi, Y. Yang, M. Li, F. Zhang, M.-K. Zhu, S. Huang, S. Huang, Y.-W. Zhang, Q. Wang, Redox-mediated ambient electrolytic nitrogen reduction for hydrazine and ammonia generation, Angew. Chem. Int. Ed. 60 (2021) 18721–18727, https://doi.org/10.1002/anie.202105536.

[21] K.H. Kim, C.-W. Choi, S. Choung, Y. Cho, S. Kim, C. Oh, K.-S. Lee, C.-L. Lee, K. Zhang, J.W. Han, S.-Y. Choi, J.H. Park, Continuous oxygen vacancy gradient in TiO_2 photoelectrodes by a photoelectrochemical-driven "self-purification" process, Adv. Energy Mater. 12 (2022), 2103495, https://doi.org/10.1002/aenm.202103495.

[22] M. Guo, M. Xu, Y. Qu, C. Hu, P. Yan, T.T. Isimjan, X. Yang, Electronic/mass transport increased hollow porous Cu_3P/MoP nanospheres with strong electronic interaction for promoting oxygen reduction in Zn-air batteries, Appl. Catal. B: Environ. 297 (2021), 120415, https://doi.org/10.1016/j.apcatb.2021.120415.

[23] Z. Li, J. Zhang, B.Y. Guan, X.W. Lou, Mesoporous carbon@titanium nitride hollow spheres as an efficient SeS_2 host for advanced Li–SeS_2 batteries, Angew. Chem. Int. Ed. 56 (2017) 16003–16007, https://doi.org/10.1002/anie.201709176.

[24] B.Y. Guan, L. Yu, J. Li, X.W.D. Lou, A universal cooperative assembly-directed method for coating of mesoporous TiO_2 nanoshells with enhanced lithium storage properties, Sci. Adv. 2 (2016), e1501554, https://doi.org/10.1126/sciadv.1501554.

[25] S. Zhao, H.-X. Liu, Y. Qiu, S.-Q. Liu, J.-X. Diao, C.-R. Chang, R. Si, X.-H. Guo, An oxygen vacancy-rich two-dimensional Au/TiO_2 hybrid for synergistically enhanced electrochemical N_2 activation and reduction, J. Mater. Chem. A 8 (2020) 6586–6596, https://doi.org/10.1039/D0TA00658K.

[26] J.-G. Li, T. Ishigaki, Brookite→rutile phase transformation of TiO_2 studied with monodispersed particles, Acta Mater. 52 (2004) 5143–5150, https://doi.org/10.1016/j.actamat.2004.07.020.

[27] B. Liu, L. Huo, Z. Gao, G. Zhi, G. Zhang, J. Zhang, Graphene decorated with uniform ultrathin $(CoP)_x$-$(FeP)_{1-x}$ nanorods: a robust non-noble-metal catalyst for hydrogen evolution, Small 13 (2017), 1700092, https://doi.org/10.1002/smll.201700092.

[28] Q. Zhou, Z. Zhang, J. Cai, B. Liu, Y. Zhang, X. Gong, X. Sui, A. Yu, L. Zhao, Z. Wang, Z. Chen, Template-guided synthesis of Co nanoparticles embedded in hollow nitrogen doped carbon tubes as a highly efficient catalyst for rechargeable Zn-air batteries, Nano Energy 71 (2020), 104592, https://doi.org/10.1016/j.nanoen.2020.104592.

[29] J. Zhu, Q. He, Y. Liu, J. Key, S. Nie, M. Wu, P.K. Shen, Three-dimensional, hetero-structured, Cu_3P@C nanosheets with excellent cycling stability as Na-ion battery anode material, J. Mater. Chem. A 7 (2019) 16999–17007, https://doi.org/10.1039/C9TA04035H.

[30] Y. Wang, X. Li, M. Zhang, J. Zhang, Z. Chen, X. Zheng, Z. Tian, N. Zhao, X. Han, K. Zaghib, Y. Wang, Y. Deng, W. Hu, Highly active and durable single-atom tungsten-doped $NiS_{0.5}Se_{0.5}$ nanosheet @ $NiS_{0.5}Se_{0.5}$ nanorod heterostructures for water splitting, Adv. Mater. 34 (2022), 2107053, https://doi.org/10.1002/adma.202107053.

[31] D.C. Nguyen, T.L.L. Doan, S. Prabhakaran, D.H. Kim, N.H. Kim, J.H. Lee, Rational construction of Au@$Co_2N_{0.67}$ nanodots-interspersed 3D interconnected N-graphene hollow sphere network for efficient water splitting and Zn-air battery, Nano Energy 89 (2021), 106420, https://doi.org/10.1016/j.nanoen.2021.106420.

[32] P. Xu, K. Dai, C. Yang, X. Wang, R. Zou, J. Shao, G. Zeng, M. Zhang, Q. Huang, Z. Su, Efficient synthesis of Cu_3P nanoparticles confined in 3D nitrogen-doped carbon networks as high performance anode for lithium/sodium-ion batteries, J. Alloy. Compd. 849 (2020), 156436, https://doi.org/10.1016/j.jallcom.2020.156436.

[33] Y. Wu, Z. Gao, Y. Feng, Q. Cui, C. Du, C. Yu, L. Liang, W. Zhao, J. Feng, J. Sun, R. Yang, J. Sun, Harnessing selective and durable electrosynthesis of H_2O_2 over dual-defective yolk-shell carbon nanosphere toward on-site pollutant degradation, Appl. Catal. B: Environ. 298 (2021), 120572, https://doi.org/10.1016/j.apcatb.2021.120572.

[34] X. Zhao, X. Yu, S. Xin, S. Chen, C. Bao, W. Xu, J. Xue, B. Hui, J. Zhang, X. She, D. Yang, Enhanced oxygen reduction reaction for Zn-air battery at defective carbon fibers derived from seaweed polysaccharide, Appl. Catal. B: Environ. 301 (2022), 120785, https://doi.org/10.1016/j.apcatb.2021.120785.

[35] R. Santhosh Kumar, S. Ramakrishnan, S. Prabhakaran, A.R. Kim, D.R. Kumar, D. H. Kim, D.J. Yoo, Structural, electronic, and electrocatalytic evaluation of spinel transition metal sulfide supported reduced graphene oxide, J. Mater. Chem. A 10 (2022) 1999–2011, https://doi.org/10.1039/D1TA08224H.

[36] X. Liu, Y. Zhang, Z. Zhao, H. Gao, J. Kang, R. Wang, G. Ge, X. Jia, Highly exposed discrete Co atoms anchored in ultrathin porous N, P-codoped carbon nanosheets for efficient oxygen electrocatalysis and rechargeable aqueous/solid-state Zn–air batteries, J. Mater. Chem. A 9 (2021) 22643–22652, https://doi.org/10.1039/D1TA07404K.

[37] H. Wang, Y. Jiao, S. Wang, P. Ye, J. Ning, Y. Zhong, Y. Hu, Accelerating triple transport in zinc-air batteries and water electrolysis by spatially confining Co nanoparticles in breathable honeycomb-like macroporous N-doped carbon, Small 17 (2021), 2103517, https://doi.org/10.1002/smll.202103517.

[38] P. Hou, D. Li, N. Yang, J. Wan, C. Zhang, X. Zhang, H. Jiang, Q. Zhang, L. Gu, D. Wang, Delicate control on the shell structure of hollow spheres enables tunable mass transport in water splitting, Angew. Chem. Int. Ed. 60 (2021) 6926–6931, https://doi.org/10.1002/anie.202016285.

[39] D. Zhao, N. Yang, Y. Wei, Q. Jin, Y. Wang, H. He, Y. Yang, B. Han, S. Zhang, D. Wang, Sequential drug release via chemical diffusion and physical barriers enabled by hollow multishelled structures, Nat. Commun. 11 (2020) 4450, https://doi.org/10.1038/s41467-020-18177-2.

[40] Y. Sun, Y. Li, S. You, X. Li, Y. Zhang, Z. Cai, M. Liu, N. Ren, J. Zou, $Fe_3C/CoFe_2O_4$ nanoparticles wrapped in one-dimensional MIL-53(Fe)-derived carbon nanofibers as efficient dual-function oxygen catalysts, Chem. Eng. J. 424 (2021), 130460, https://doi.org/10.1016/j.cej.2021.130460.

[41] N. Logeshwaran, I.R. Panneerselvam, S. Ramakrishnan, R.S. Kumar, A.R. Kim, Y. Wang, D.J. Yoo, Quasihexagonal platinum nanodendrites decorated over CoS2-N-doped reduced graphene oxide for electro-oxidation of C1-, C2-, and C3-type alcohols, Adv. Sci. 9 (2022), 2105344, https://doi.org/10.1002/advs.202105344.

[42] X. Zhang, X. Wen, C. Pan, X. Xiang, C. Hao, Q. Meng, Z.Q. Tian, P.K. Shen, S. P. Jiang, N species tuning strategy in N, S co-doped graphene nanosheets for electrocatalytic activity and selectivity of oxygen redox reactions, Chem. Eng. J. 431 (2022), 133216, https://doi.org/10.1016/j.cej.2021.133216.

[43] F. Li, T. Qin, Y. Sun, R. Jiang, J. Yuan, X. Liu, A.P. O'Mullane, Preparation of a one-dimensional hierarchical MnO@CNT@Co–N/C ternary nanostructure as a high-performance bifunctional electrocatalyst for rechargeable Zn–air batteries, J. Mater. Chem. A 9 (2021) 22533–22543, https://doi.org/10.1039/D1TA07259E.

[44] Y. Park, H. Sim, M. Jo, G.Y. Kim, D. Yoon, H. Han, Y. Kim, K. Song, D. Lee, S. Y. Choi, J. Son, Directional ionic transport across the oxide interface enables low-temperature epitaxy of rutile TiO_2, Nat. Commun. 11 (2020) 1401, https://doi.org/10.1038/s41467-020-15142-x.

[45] K.M. Naik, E. Higuchi, H. Inoue, Pt nanoparticle-decorated two-dimensional oxygen-deficient TiO_2 nanosheets as an efficient and stable electrocatalyst for the hydrogen evolution reaction, Nanoscale 12 (2020) 11055–11062, https://doi.org/10.1039/D0NR02092C.

[46] J. Tian, Q. Liu, N. Cheng, A.M. Asiri, X. Sun, Self-supported Cu_3P nanowire arrays as an integrated high-performance three-dimensional cathode for generating hydrogen from water, Angew. Chem. Int. Ed. 53 (2014) 9577–9581, https://doi.org/10.1002/anie.201403842.

[47] J. Li, X. Li, P. Liu, X. Zhu, R.N. Ali, H. Naz, Y. Yu, B. Xiang, Self-supporting hybrid fiber mats of Cu_3P–Co_2P/N–C endowed with enhanced lithium/sodium ions storage performances, ACS Appl. Mater. Interfaces 11 (2019) 11442–11450, https://doi.org/10.1021/acsami.8b22367.

[48] Y. Yu, M. Yan, W.-D. Dong, L. Wu, Y.-W. Tian, Z. Deng, L.-H. Chen, T. Hasan, Y. Li, B.-L. Su, Optimizing inner voids in yolk-shell TiO_2 nanostructure for high-performance and ultralong-life lithium-sulfur batteries, Chem. Eng. J. 417 (2021), 129241, https://doi.org/10.1016/j.cej.2021.129241.

[49] C.-F. Li, L.-J. Xie, J.-W. Zhao, L.-F. Gu, H.-B. Tang, L. Zheng, G.-R. Li, Interfacial Fe−O−Ni−O−Fe bonding regulates the active Ni Sites of Ni-MOFs via iron doping and decorating with FeOOH for super-efficient oxygen evolution, Angew. Chem. Int. Ed. (2022), e202116934, https://doi.org/10.1002/anie.202116934.

[50] X. Zhang, J. Yan, L.Y.S. Lee, Highly promoted hydrogen production enabled by interfacial PN chemical bonds in copper phosphosulfide Z-scheme composite, Appl. Catal. B: Environ. 283 (2021), 119624, https://doi.org/10.1016/j.apcatb.2020.119624.

[51] J. Song, Y. Chen, H. Huang, J. Wang, S.-C. Huang, Y.-F. Liao, A.E. Fetohi, F. Hu, H.-Y. Chen, L. Li, X. Han, K.M. El-Khatib, S. Peng, Heterointerface engineering of hierarchically assembling layered double hydroxides on cobalt selenide as efficient trifunctional electrocatalysts for water splitting and zinc-air battery, Adv. Sci. 9 (2022), 2104522, https://doi.org/10.1002/advs.202104522.

[52] Q. Yue, T. Gao, S. Wu, H. Yuan, D. Xiao, Ultrafast fabrication of robust electrocatalyst having Fe/Fe_3C and CuNC for enhanced oxygen reduction reaction activity, J. Colloid Interface Sci. 605 (2022) 906–915, https://doi.org/10.1016/j.jcis.2021.07.125.

[53] W. Zhai, S. Huang, C. Lu, X. Tang, L. Li, B. Huang, T. Hu, K. Yuan, X. Zhuang, Y. Chen, Simultaneously integrate iron single atom and nanocluster triggered tandem effect for boosting oxygen electroreduction, Small (2022), 2107225, https://doi.org/10.1002/smll.202107225.

[54] H. Xu, H. Jia, H. Li, J. Liu, X. Gao, J. Zhang, M. Liu, D. Sun, S. Chou, F. Fang, R. Wu, Dual carbon-hosted Co-N_3 enabling unusual reaction pathway for efficient oxygen reduction reaction, Appl. Catal. B: Environ. 297 (2021), 120390, https://doi.org/10.1016/j.apcatb.2021.120390.

[55] S.-Y. Lin, L.-X. Xia, Y. Cao, H.-L. Meng, L. Zhang, J.-J. Feng, Y. Zhao, A.-J. Wang, Electronic regulation of ZnCo dual-atomic active sites entrapped in 1D@2D hierarchical N-doped carbon for efficient synergistic catalysis of oxygen reduction in Zn–Air battery, Small (2022), 2107141, https://doi.org/10.1002/smll.202107141.

[56] J. Liu, J. Zhou, M.K.H. Leung, Valence engineering of polyvalent cobalt encapsulated in a carbon nanofiber as an efficient trifunctional electrocatalyst for the Zn–air battery and overall water splitting, ACS Appl. Mater. Interfaces 14 (2022) 4399–4408, https://doi.org/10.1021/acsami.1c18384.

[57] W. Fu, Y. Wang, J. Hu, H. Zhang, P. Luo, F. Sun, X. Ma, Z. Huang, J. Li, Z. Guo, Y. Wang, Surface-electron coupling for efficient hydrogen evolution, Angew. Chem. Int. Ed. 58 (2019) 17709–17717, https://doi.org/10.1002/anie.201908938.

[58] X. Zhuang, Y. Zhou, Z. Jiang, X. Yao, X.-Y. Yu, Synergetic electronic modulation and nanostructure engineering of heterostructured RuO_2/Co_3O_4 as advanced bifunctional electrocatalyst for zinc–air batteries, J. Mater. Chem. A 9 (2021) 26669–26675, https://doi.org/10.1039/D1TA09278B.

[59] Y. Wu, C. Ye, L. Yu, Y. Liu, J. Huang, J. Bi, L. Xue, J. Sun, J. Yang, W. Zhang, X. Wang, P. Xiong, J. Zhu, Soft template-directed interlayer confinement synthesis of a Fe-Co dual single-atom catalyst for Zn-air batteries, Energy Storage Mater. 45 (2022) 805–813, https://doi.org/10.1016/j.ensm.2021.12.029.

[60] Y. Guo, J. Tang, H. Qian, Z. Wang, Y. Yamauchi, One-pot synthesis of zeolitic imidazolate framework 67-derived hollow Co_3S_4@MoS_2 heterostructures as efficient bifunctional catalysts, Chem. Mater. 29 (2017) 5566–5573, https://doi.org/10.1021/acs.chemmater.7b00867.

[61] R. Boppella, J. Tan, W. Yang, J. Moon, Homologous CoP/NiCoP heterostructure on N-doped carbon for highly efficient and pH-universal hydrogen evolution electrocatalysis, Adv. Funct. Mater. 29 (2018), 1807976, https://doi.org/10.1002/adfm.201807976.